

Article

Deep Red Photoluminescence from Cr³⁺ in Fluorine-Doped Lithium Aluminate Host Material

Yuki Kamada ¹, Ryusei Hayasaka ¹, Kento Uchida ¹, Taisei Suzuki ¹, Takahiro Takei ² , Mamoru Kitaura ³ , Hiroko Kominami ⁴, Kazuhiko Hara ⁵ and Yuta Matsushima ^{1,*} 

¹ Applied Chemistry, Chemical Engineering, and Biochemical Engineering, Yamagata University, Yonezawa 992-8510, Japan

² Center for Crystal Science and Technology, University of Yamanashi, Kofu 400-0021, Japan; takei@yamanashi.ac.jp

³ Faculty of Science, Yamagata University, Yamagata 990-8560, Japan; kitaura@sci.kj.yamagata-u.ac.jp

⁴ Faculty of Engineering, Shizuoka University, Hamamatsu 432-8561, Japan; kominami.hiroko@shizuoka.ac.jp

⁵ Research Institute of Electronics, Shizuoka University, Hamamatsu 432-8011, Japan; hara.kazuhiko@shizuoka.ac.jp

* Correspondence: ymatsush@yz.yamagata-u.ac.jp; Tel.: +81-238-26-3165

Abstract: Deep red phosphors have attracted much attention for their applications in lighting, medical diagnosis, health monitoring, agriculture, etc. A new phosphor host material based on fluorine-doped lithium aluminate (ALFO) was proposed and deep red emission from Cr³⁺ in this host material was demonstrated. Cr³⁺ in ALFO was excited by blue (~410 nm) and green (~570 nm) rays and covered the deep red to near-infrared region from 650 nm to 900 nm with peaks around 700 nm. ALFO was a fluorine-doped form of the spinel-type compound LiAl₅O₈ with slightly Li-rich compositions. The composition depended on the preparation conditions, and the contents of Li and F tended to decrease with preparation temperature, such as Al_{4.69}Li_{1.31}F_{0.28}O_{7.55} at 1100 °C, Al_{4.73}Li_{1.27}F_{0.17}O_{7.65} at 1200 °C, and Al_{4.83}Li_{1.17}F_{0.10}O_{7.78} at 1300 °C. The Rietveld analysis revealed that ALFO and LiAl₅O₈ were isostructural with respect to the spinel-type lattice and in a disorder–order relationship in the arrangement of Li⁺ and Al³⁺. The emission peak of Cr³⁺ in LiAl₅O₈ resided at 716 nm, while Cr³⁺ in ALFO showed a rather broad doublet peak with the tops at 708 nm and 716 nm when prepared at 1200 °C. The broad emission peak indicated that the local environment around Cr³⁺ in ALFO was distorted, which was also supported by electron spin resonance spectra, suggesting that the local environment around Cr³⁺ in ALFO was more inhomogeneous than expected from the diffraction-based structural analysis. It was demonstrated that even a small amount of dopant (in this case fluorine) could affect the local environment around luminescent centers, and thus the luminescence properties.

Keywords: deep red phosphor; fluorine-doped lithium aluminate; spinel compound; disordered spinel; 3d transition metal ion



Citation: Kamada, Y.; Hayasaka, R.; Uchida, K.; Suzuki, T.; Takei, T.; Kitaura, M.; Kominami, H.; Hara, K.; Matsushima, Y. Deep Red Photoluminescence from Cr³⁺ in Fluorine-Doped Lithium Aluminate Host Material. *Materials* **2024**, *17*, 338. <https://doi.org/10.3390/ma17020338>

Academic Editor: Heesun Yang

Received: 1 December 2023

Revised: 25 December 2023

Accepted: 2 January 2024

Published: 10 January 2024



Copyright: © 2024 by the authors. Licensee MDPI, Basel, Switzerland. This article is an open access article distributed under the terms and conditions of the Creative Commons Attribution (CC BY) license (<https://creativecommons.org/licenses/by/4.0/>).

1. Introduction

Inorganic phosphors have been widely used in display and lighting applications such as cathode-ray tubes and fluorescent lamps. Conventional phosphors used in these applications are typically excited by high-energy radiation such as X-rays and ultraviolet (UV) rays or electron beams. Recent light-emitting diode (LED) lighting achieves a pseudo-white color by combining blue light emitted from LED chips and the emission of the phosphors excited by the blue light, which has lower energy than X-rays and UV rays.

“Red” is an important color in lighting applications because it has a significant emotional effect on humans, as people unconsciously perceive the warmth of an atmosphere, the state of a person’s health from their complexion, or the freshness of red meat from the color red. Typical rare-earth ions that emit red light are Eu³⁺ and Eu²⁺. The former shows

orange-red luminescence with a sharp peak around 610 nm due to the 4f-4f transition in some host materials, while the latter, e.g., $\text{CaAlSiN}_3\text{:Eu}^{2+}$ [1–3] and $\text{K}_2\text{CaPO}_4\text{:Eu}^{2+}$ [4], shows a rather broad emission between 600 and 700 nm due to the 5d-4f transition. In recent years, fluorescent materials other than inorganic phosphors, such as polymethine dye molecules, their aggregates and nanoparticles, conjugated polymer nanoparticles, single-walled carbon nanotubes, quantum dots, and lanthanide complex molecules, have also been extensively investigated for emerging applications utilizing near-infrared emission from 700 to 2000 nm, including medical diagnosis, health monitoring, agriculture, and night vision [5–8].

The 3d transition metal ions, Cr^{3+} , Mn^{4+} , and Fe^{3+} , can act as luminescent centers emitting in the red to deep red region from 640 to 800 nm in suitable host materials due to 3d-3d transitions [9]. The luminescence properties are highly dependent on the combination of the luminescent center ions and the host materials. For example, Mn^{4+} in K_2SiF_6 has sharp excitation lines around 450 nm, leading it to be a candidate for a red phosphor for LED lighting [10]. On the other hand, Mn^{4+} in SrLaAlO_4 [11] and SrGdAlO_4 [12] is not excited by blue light as it shows the excitation peak in the UV region around 365 nm.

Cr^{3+} has specifically attracted attention as a luminescent center for near-infrared luminescence. Various compounds, whether natural or synthetic, have been reported as host materials, in which Cr^{3+} often replaces Al^{3+} or Ga^{3+} in the host compounds. The sharp deep red emission around 694 nm of Cr^{3+} in $\alpha\text{-Al}_2\text{O}_3$ has been utilized for solid-state lasers. Emission of Cr^{3+} has also been observed in, for example, $\beta\text{-Ga}_2\text{O}_3$ [13], spinel-type MgAl_2O_4 [14–16], ZnAl_2O_4 [15–18], LiAl_5O_8 [19,20], garnet-type $\text{Y}_3\text{Al}_5\text{O}_{12}$ [21–23], $\text{Gd}_3\text{Ga}_5\text{O}_{12}$ [24], and $\text{Gd}_3\text{Sc}_2\text{Ga}_3\text{O}_{12}$ [22], beryl $\text{Be}_3\text{Al}_2\text{Si}_6\text{O}_{18}$ [25,26], aluminosilicate $\text{CaSc}_{1-x}\text{Al}_{1+x}\text{SiO}_6$ [27], $\text{SrAl}_{11.88-x}\text{Ga}_x\text{O}_{19}$ [28], $\text{Bi}_2\text{Ga}_4\text{O}_9$ [29], $\text{La}_3\text{GaGe}_5\text{O}_{16}$ [30], and phosphate KMPO_7 ($M = \text{Ga}, \text{Sc}, \text{In}, \text{and Lu}$) [31]. Cr^{3+} in these host materials has been considered to occupy octahedral sites. When the strength of the crystal field is relatively large, such as $\alpha\text{-Al}_2\text{O}_3$ and the spinel-type hosts [14–20], sharp emission spectra are observed near 700 nm due to the electronic transition from the excited state 2E to the ground state 4A_2 , while in the host materials with a weak crystal field, such as the garnet-type hosts [21–24], $\text{CaSc}_{1-x}\text{Al}_{1+x}\text{SiO}_6$ [27], $\text{Bi}_2\text{Ga}_4\text{O}_9$ [29], and $\text{La}_3\text{GaGe}_5\text{O}_{16}$ [30], a red-shifted broad emission is observed due to the spin-allowed ${}^4T_2 \rightarrow {}^4A_2$ transition.

We have demonstrated different types of deep red luminescence from 650 to 800 nm achieved with a single host material doped with either Mn^{4+} , Fe^{3+} , or Cr^{3+} [32]. The host material was prepared from LiF and Al_2O_3 at 1:2, which first appeared in the report by Belov et al. [33], described as “ $\text{Al}_4\text{LiO}_6\text{F}$ ” with a spinel-type lattice, assuming a stoichiometric reaction between LiF and two Al_2O_3 . Our previous paper and other researchers referred to this material as $\text{Al}_4\text{LiO}_6\text{F}$ [34] or $\text{LiAl}_4\text{O}_6\text{F}$ [35], following Belov’s suggestion. However, the composition of $\text{Al}_4\text{LiO}_6\text{F}$ does not match the spinel-type composition of AB_2O_4 . In normal spinel, the divalent cation A^{2+} and the trivalent cation B^{3+} occupy the tetrahedral and octahedral cation sites in the spinel-type lattice.

In our previous paper [32], we showed that Mn^{4+} in the host material prepared from LiF and Al_2O_3 significantly enhanced photoluminescence (PL) compared to spinel-type lithium aluminate LiAl_5O_8 , indicating its potential as a new host material for deep red phosphors. However, the details of the composition and crystal structure had not been clarified. In this paper, we denote this host material as aluminum lithium fluoride oxide (ALFO) and discuss the characteristics of ALFO and the luminescent properties of Cr^{3+} in ALFO, the luminescent center ion for deep red phosphors which can be excited by visible radiation; this finding will help provide new insights into the design of new phosphor host materials.

2. Materials and Methods

ALFO samples were prepared from LiF and $\gamma\text{-Al}_2\text{O}_3$; LiF was prepared from lithium hydroxide monohydrate (99%, Kanto Chem. Co., Inc., Tokyo, Japan) and ammonium fluoride (99%, Kanto Chem. Co., Inc.) by precipitation in aqueous solution. The starting

aluminum source was aluminum triisopropoxide (>99.9%, Kanto Chem. Co., Inc.); aluminum hydroxide was precipitated at pH 10 in isopropanol solution by NH_3 aq. Using $\text{Cr}(\text{NO}_3)_3 \cdot 9\text{H}_2\text{O}$ (98.0–103.0%, Kanto Chem. Co., Inc.) as the starting material, Cr^{3+} was coprecipitated with aluminum hydroxide in the isopropanol solution. The coprecipitated hydroxide mixture was rinsed with deionized water, heated in a platinum crucible to 1000 °C at a ramp rate of 10 °C/min, and cooled in the furnace to obtain $\gamma\text{-Al}_2\text{O}_3:\text{Cr}^{3+}$. The concentration of Cr^{3+} was defined as $\text{Cr}^{3+}/(\text{Al}^{3+} + \text{Cr}^{3+})$, assuming that it replaced Al^{3+} in the products. $\gamma\text{-Al}_2\text{O}_3:\text{Cr}^{3+}$ and LiF were weighed at $(\text{Al} + \text{Cr})/\text{Li} = 4$ (note that $\gamma\text{-Al}_2\text{O}_3$ contains a certain amount of water in its composition and that $(\text{Al} + \text{Cr})/\text{Li}$ in the starting composition could be slightly smaller than 4). Typically, 0.2 g of a mixture of LiF and $\gamma\text{-Al}_2\text{O}_3:\text{Cr}^{3+}$ was placed in a 5 cm³ platinum crucible with a lid. The 5 cm³ platinum crucible was put in a larger platinum crucible (30 cm³) with a lid to suppress volatilization of the components, specifically lithium and fluorine, during heat treatment. Samples were heated at 800–1300 °C at a ramp rate of 20 °C/min. Heating times were 15 min at 1100 °C and above, and 1 h at 800–1000 °C.

For comparison, $\text{LiAl}_5\text{O}_8:\text{Cr}^{3+}$ was prepared from Li_2CO_3 (99%, Kanto Chem. Co., Inc.) and $\alpha\text{-Al}_2\text{O}_3:\text{Cr}^{3+}$ at a ratio of $\text{Li}:(\text{Al} + \text{Cr}) = 1:5$. $\alpha\text{-Al}_2\text{O}_3$ was prepared by heating the $\text{Al}(\text{OH})_3$ precipitate at 1200 °C for 2 h in air. The Li and Al sources were thoroughly mixed in an alumina mortar and pressed into pellets. The pellets were heated in an alumina crucible with the inner bottom covered with pre-prepared LiAl_5O_8 powder to suppress the diffusion of the lithium component from the sample to the alumina crucible.

The chemical compositions of the samples were analyzed for Li, Al, and Cr using inductively coupled plasma-optical emission spectroscopy after the samples were decomposed in molten salt. Fluorine contents were analyzed by ion chromatography after thermal hydrolysis. Oxygen contents were estimated from charge neutrality using the analyzed Al^{3+} , Li^+ , Cr^{3+} , and F^- contents. The morphology of the phosphor particles was observed with scanning electron microscopy (SEM) (T-330, JEOL Ltd., Tokyo, Japan and TM3030 plus, Hitachi High-Tech Co., Tokyo, Japan). Carbon was evaporated for conductive coating on the samples.

The crystallographic phases were identified by X-ray diffraction (XRD) using $\text{Cu K}\alpha$ radiation (MiniFlex, Rigaku Co., Tokyo, Japan) operated at 40 kV and 15 mA. The scan step was 0.01°. Structural refinement was carried out by the Rietveld method using Rietan-FP [36]. The crystal structures were illustrated using VESTA [37]. The PL spectra and the photoluminescence excitation (PLE) spectra were measured using a fluorescence spectrometer (FL-6000, Shimadzu Co., Kyoto, Japan) and a multichannel spectral analyzer (PMA-11, Hamamatsu Photonics Co., Hamamatsu, Japan) combined with a lamp and a bandpass filter (MC-570, Asahi Spectra Co. Ltd., Tokyo, Japan) as the excitation light source. Quantum efficiencies (QEs) were evaluated with FL-6000 using an integral sphere. X-band (9.13 GHz) electron spin resonance (ESR) measurements were conducted at room temperature between 0 and 800 mT with 100 kHz magnetic field modulation to detect differences in the local environments around Cr^{3+} in the different host materials. As an aid for the discussion of the ESR results, classical molecular dynamics (MD) simulations using the MXDORTO code [38] were performed to reproduce the local structures. One Cr^{3+} ion was introduced into an octahedral site in the MD cell to replace the Al^{3+} ion, and the MD cell consisted of the crystallographic unit cells with x , y , and z axes of 23–26 Å. The detailed calculation procedure of the MD has already been described in our previous paper [39].

3. Results and Discussion

3.1. Compositions and Crystal Structure

Figure 1 compares the XRD patterns of $\text{ALFO}:\text{Cr}^{3+}$ and $\text{LiAl}_5\text{O}_8:\text{Cr}^{3+}$ prepared at 1200 °C with the Cr^{3+} concentration of 0.5%. Each pattern is consistent with the single phase of LiAl_5O_8 (ICDD # 38-1426) and $\text{Al}_4\text{LiO}_6\text{F}$ (ICDD #38-610) reported by Belov et al. [33]. The peaks marked with ▼ are the extra peaks originating from the cation ordering of Li^+ and Al^{3+} in spinel-type LiAl_5O_8 , which will be discussed below.

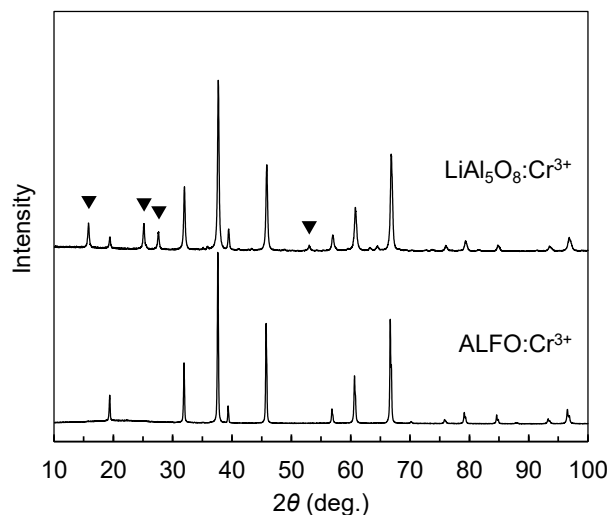


Figure 1. Comparison of XRD patterns of ALFO:Cr³⁺ and LiAl₅O₈:Cr³⁺ prepared at 1200 °C. The peaks marked with ▼ are the extra peaks originating in the cation ordering of Li⁺ and Al³⁺ in the spinel-type lattice of LiAl₅O₈ (see text for details).

Table 1 shows the chemical compositions of the ALFO host material without the luminescent center ion Cr³⁺ prepared at 1100 °C, 1200 °C, and 1300 °C. The XRD patterns of these samples are shown in Figure S1 in Supplementary Materials, confirming that each sample was in the single phase. The composition suggested by Belov et al. [33] was Al₄LiO₆F, but the compositional analysis (Table 1) showed that ALFO is a fluorine-doped form of LiAl₅O₈ with Li-rich compositions. The Al/Li/F ratios varied depending on the preparation temperature. The fluorine content was 0.28 for the sample prepared at 1100 °C; it decreased to 0.10 for the sample prepared at 1300 °C, indicating that fluorine dissipated during heat treatment at the high temperatures. The lithium content also decreased from Al/Li = 4.69/1.31 (=3.58/1) at 1100 °C and 4.73/1.27 (=3.72/1) at 1200 °C to 4.83/1.17 (=4.13/1) at 1300 °C.

Table 1. Chemical compositions of the fluorine-doped lithium aluminate (ALFO) host material prepared at different temperatures.

| Preparation Temperature | Chemical Composition |
|-------------------------|---|
| 1100 °C | Al _{4.69} Li _{1.31} F _{0.28} O _{7.55} |
| 1200 °C | Al _{4.73} Li _{1.27} F _{0.17} O _{7.65} |
| 1300 °C | Al _{4.83} Li _{1.17} F _{0.10} O _{7.78} |

The Cr³⁺ concentration in the Cr³⁺-doped ALFO samples was consistent with the starting composition; the compositional analysis showed that ALFO:Cr³⁺ prepared at 1200 °C with a starting concentration of 0.5% Cr³⁺ was 0.48%.

The structural refinement by the Rietveld analysis for ALFO prepared at 1200 °C without Cr³⁺ converged to $R_{wp}/R_p = 0.058/0.042$, goodness-of-fit (S) = 1.90, and the lattice constant $a = 7.9222(8)$ Å. Figure S2 in Supplementary Materials shows the refinement results and the structural parameters are listed in Table S1 in Supplementary Materials. The structural model was based on disordered spinel with the space group $Fd\bar{3}m$. The spinel-type lattice accommodates cations in the tetrahedral and octahedral sites. In the initial model, Al³⁺ and Li⁺ were assumed to be randomly distributed in the tetrahedral sites ($8a$ position) and the octahedral sites ($16d$ position). For the random distribution, the occupancies (g) of Li estimated from the chemical composition analysis (Table 1) should be $g = 0.211$ for both the tetrahedral and octahedral sites. However, the refined structure indicated a slight preference for Li to occupy the octahedral site, with $g = 0.183$ and 0.226 for the tetrahedral and octahedral sites, respectively.

According to the literature, LiAl_5O_8 has crystallographic polymorphs, namely I (disordered) and II (ordered) [19,40–42] (Appendix A). Figure 2 compares the crystal structures of ALFO and ordered LiAl_5O_8 . Figure S3 in Supplementary Materials illustrates the structural differences in the arrangement of the tetrahedra and the octahedra in the range of $x = 0.2$ to 0.6 for spinel-type ALFO and ordered LiAl_5O_8 in a perspective view along $\langle 100 \rangle$. The octahedra form diagonal chains by edge sharing, and the chains of the octahedra are linked to each other by the tetrahedra connected by corner sharing. In ordered LiAl_5O_8 , the tetrahedra consist of only AlO_4 , and the chains of the octahedra consist of one LiO_6 and three AlO_6 in sequence (Figure 2a and Figure S3a in Supplementary Materials). In ALFO, on the other hand, the tetrahedra are statistically AlO_4 or LiO_4 and the octahedra are AlO_6 or LiO_6 (Figure 2b and Figure S3b in Supplementary Materials).

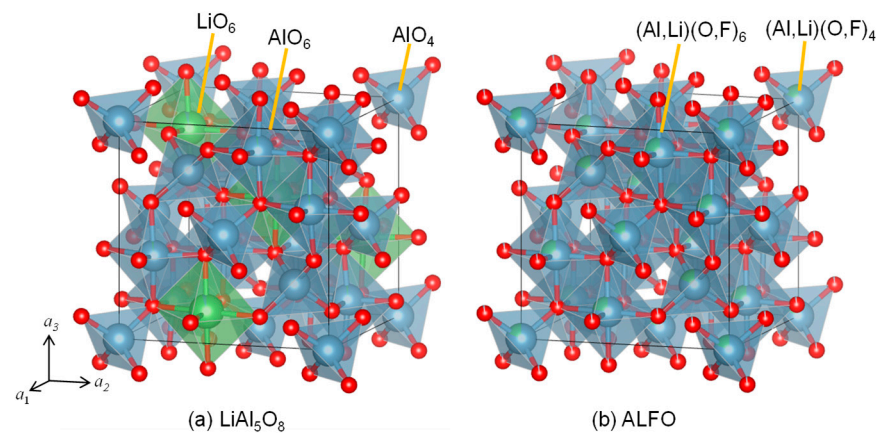


Figure 2. Crystal structures of (a) ordered LiAl_5O_8 and (b) aluminum lithium fluoride oxide (ALFO) after Rietveld analysis.

The spinel-type framework leads to the unmarked peaks common to ALFO and LiAl_5O_8 in the XRD patterns in Figure 1. The peaks marked with ▼ in Figure 1 are derived from the periodicity due to the regular arrangement of Al^{3+} and Li^+ on the cation sites in ordered LiAl_5O_8 . The difference in the cation arrangement results in the lattice symmetry of $Fd\bar{3}m$ for ALFO and $P4_332$ for ordered LiAl_5O_8 . The doped Cr^{3+} was assumed to occupy octahedral sites in both the host materials because of the preference of Cr^{3+} with the d^3 configuration to occupy octahedral sites; the ionic radius of Cr^{3+} on a tetrahedral site is not defined in Shannon’s ionic radii table [43].

As a summary of the compositional and structural analyses, ALFO and ordered LiAl_5O_8 have a disorder–order relationship with respect to the arrangement of Li^+ and Al^{3+} on the cation sites. ALFO has slightly Li-rich compositions than LiAl_5O_8 , resulting in anion vacancies for the charge neutrality. Fluorine replaces 1.3–3.5% of the oxygen sites.

The solubility limit of Cr^{3+} in the ALFO lattice exceeded 10%. Figure S4 in Supplementary Materials shows the XRD patterns of $\text{ALFO}:\text{Cr}^{3+}$ prepared at 1200 °C at different Cr^{3+} concentrations from 0.01 to 10%. All the samples were substantially a single phase of ALFO; the six-fold coordinated ionic radii of Al^{3+} and Cr^{3+} were 0.535 Å and 0.615 Å [43], and replacing Al^{3+} with larger Cr^{3+} shifted the diffraction peaks slightly toward the lower angles.

3.2. Morphologies

Figure 3 shows the SEM images of 0.5% Cr^{3+} -doped ALFO and LiAl_5O_8 prepared at 1200 °C and 1300 °C. The effect of treatment temperature did not appear to have a significant effect on the morphology; $\text{ALFO}:\text{Cr}^{3+}$ was composed of angular grains with well-developed crystal faces. The grain size varied from sub-micrometers to several micrometers. On the other hand, the grains of $\text{LiAl}_5\text{O}_8:\text{Cr}^{3+}$ did not have a definite shape and their size was several hundred nanometers, which formed agglomerates of a few micrometers in size. The difference in morphology between $\text{ALFO}:\text{Cr}^{3+}$ and $\text{LiAl}_5\text{O}_8:\text{Cr}^{3+}$ was attributed to the difference in the lithium sources. The melting points of LiF and Li_2CO_3 used to prepare

ALFO and LiAl_5O_8 are 848 °C and 723 °C, respectively. The development of the crystal faces of the ALFO:Cr^{3+} grains strongly suggested that LiF formed the melt at elevated temperatures and acted as a self-flux to grow the crystalline grains. On the other hand, the indistinct shape of the grains observed in Figure 3c,d for $\text{LiAl}_5\text{O}_8:\text{Cr}^{3+}$ indicated that no flux growth effect was expected, and thus Li_2CO_3 reacted with $\alpha\text{-Al}_2\text{O}_3:\text{Cr}^{3+}$ to form $\text{LiAl}_5\text{O}_8:\text{Cr}^{3+}$ before forming the melt.

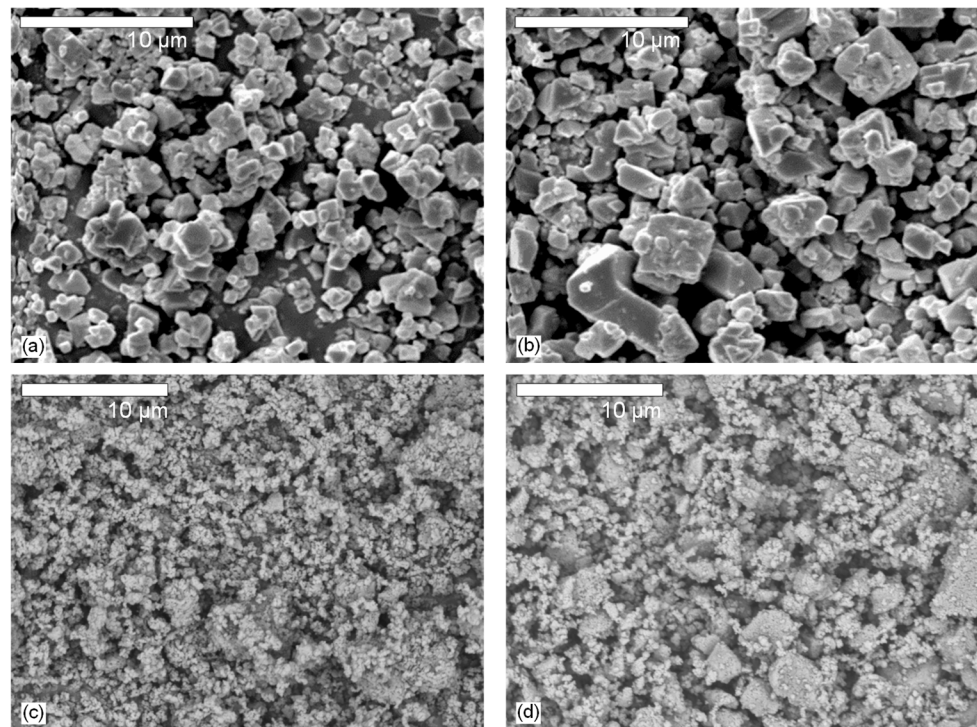


Figure 3. SEM images of aluminum lithium fluoride oxide (ALFO) (a,b) and LiAl_5O_8 (c,d). The preparation temperatures were 1200 °C for (a,c) and 1300 °C for (b,d).

3.3. Photoluminescence Properties

The emission and excitation spectra of 0.5% Cr^{3+} in ALFO, LiAl_5O_8 , and $\alpha\text{-Al}_2\text{O}_3$ prepared at 1200 °C are compared in Figure 4. The excitation spectra were similar to each other regardless of the type of the host crystal, and the excitation bands consisted of two broad peaks at around 420 nm and 570 nm. They corresponded to the transitions from the ground state 4A_2 to the excitation states $^4T_1(^4F)$ and $^4T_2(^4F)$ in Cr^{3+} of the d^3 state. The emission peaks depended on the host crystal. $\alpha\text{-Al}_2\text{O}_3:\text{Cr}^{3+}$ showed a typical line spectrum, named “R line”, at 694 nm with several small side peaks on the longer wavelength side, as found in the literature [9,44]; $\text{LiAl}_5\text{O}_8:\text{Cr}^{3+}$ showed a sharp peak at 716 nm with smaller peaks at 703 nm and 730 nm which are also similar to those reported in the previous literature [19,45]. On the other hand, Cr^{3+} in ALFO characteristically exhibited a doublet peak at 708 and 716 nm, and the profile was broader than those of $\alpha\text{-Al}_2\text{O}_3$ and LiAl_5O_8 . Although the apparent difference between the crystal structures of ALFO and ordered LiAl_5O_8 shown by the Rietveld analysis was in the cation arrangement, the broad doublet peak in ALFO:Cr^{3+} indicated that the local environment around the luminescent center Cr^{3+} in ALFO was even more inhomogeneous than simply considering octahedral coordination by six neighboring oxygens.

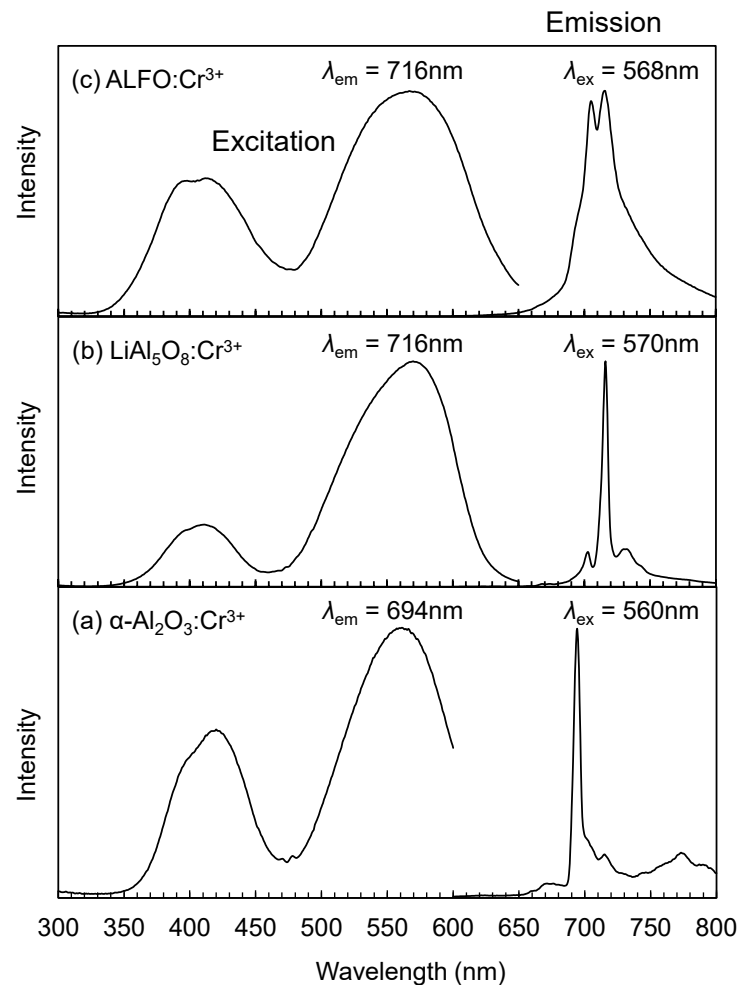


Figure 4. Emission and excitation spectra of 0.5% Cr³⁺ in α -Al₂O₃ (a), LiAl₅O₈ (b), and ALFO (c).

Figure 5 shows the variation of the emission peaks of ALFO:Cr³⁺ with the treatment temperature and compares them with those of α -Al₂O₃:Cr³⁺ and LiAl₅O₈:Cr³⁺. The peak at 696 nm of the ALFO:Cr³⁺ sample prepared at 1000 °C was due to the unreacted Al₂O₃ residue (Figure S5 in Supplementary Materials), indicating that the coprecipitated Cr³⁺ was incorporated into the α -Al₂O₃ grains to form α -Al₂O₃:Cr³⁺. The peak at around 715 nm was specific to ALFO:Cr³⁺ and was observed in ALFO:Cr³⁺ prepared at 1000–1300 °C. Interestingly, the rather broad doublet peak with peak tops at 708 nm and 716 nm was characteristically observed in the sample prepared at 1200 °C, and the detailed mechanism of the occurrence of the doublet peak is still unclear. It could be attributed to the difference in the local coordination environment around Cr³⁺ that did not appear in the average structure by XRD (Figure S5 in Supplementary Materials). Figure S5 in Supplementary Materials shows the XRD patterns of the ALFO:Cr³⁺ samples prepared at 1000–1300 °C. Residual unreacted α -Al₂O₃ was recognized in the sample prepared at 1000 °C, while the samples prepared at 1100–1300 °C were in the single phase.

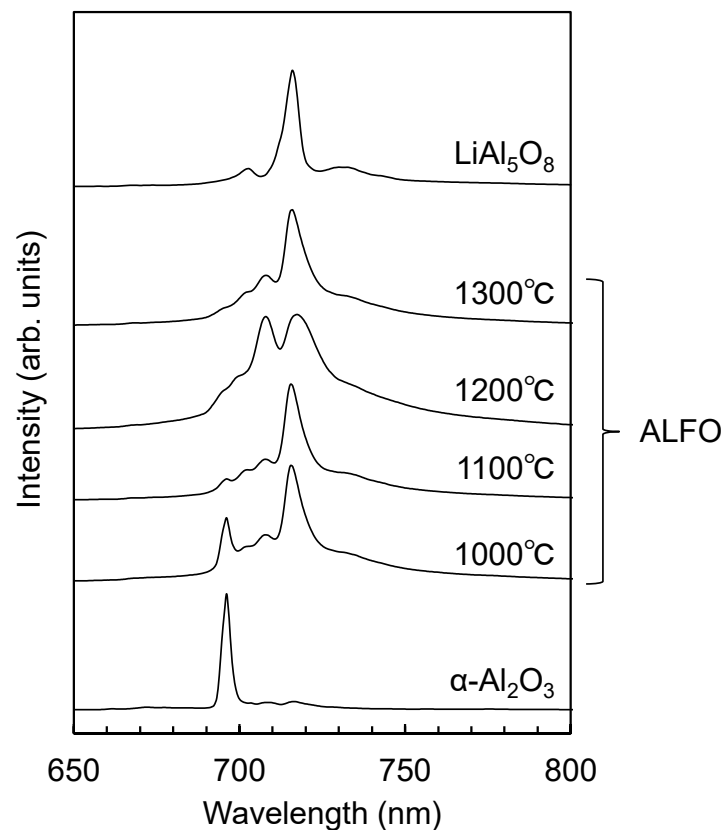


Figure 5. Variation of PL spectra of ALFO:Cr³⁺ with preparation temperature. The emission peaks of α -Al₂O₃:Cr³⁺ and LiAl₅O₈:Cr³⁺ prepared at 1200 °C are also shown for comparison.

Figure 6 compares the PL spectra of ALFO:Cr³⁺ (a) and LiAl₅O₈:Cr³⁺ (b) at different Cr³⁺ concentrations. The emission intensity of ALFO:Cr³⁺ increased from Cr³⁺ = 0.1% to 0.5% and decreased above 0.5%. Above 2.5%, the intensity of the main doublet peak decreased while the shoulders developed around 780 nm. In the previous literature, it has been discussed that the broad emission of Cr³⁺ in the near-infrared region was due either to the ${}^4T_2 \rightarrow {}^4A_2$ transition of Cr³⁺ placed in a weak crystal field, or to magnetic interactions between Cr³⁺ ions at the neighboring sites. According to the Tanabe–Sugano diagram [46–48], the first excited state in the d^3 configuration of octahedral coordination is the 4T_2 or 2E state, depending on the strength of the crystal field. The transition from the 2E state to the 4A_2 ground state yields the line spectra typically observed for Cr³⁺ around 700 nm, while broad near-infrared emission is reported for the transition from the 4T_2 state in the host materials with a weak crystal field [21–24,27,29,30]. Magnetic interactions also bring the red-shift of the emission [49], as exemplified by the so-called N-lines of Cr³⁺ emission [9,15] and the broad luminescence due to Cr³⁺-Cr³⁺ pairs observed in SrAl_{11.88-x}Ga_xO₁₉:0.12Cr³⁺ by Rajendran et al., which was concluded from the decay time measurements [28]. As for the shoulder peak around 780 nm in ALFO:Cr³⁺, the origin was attributed to the magnetic interaction between Cr³⁺ ions from the fact that the change in the lattice parameter with Cr³⁺ addition, i.e., the change in the strength of the crystal field at the Cr³⁺ sites, was not very large (Figure S4 in Supplementary Materials), and that the interaction between Cr³⁺ ions was observed in the ESR signal at a high Cr³⁺ concentration as described in Section 3.4.

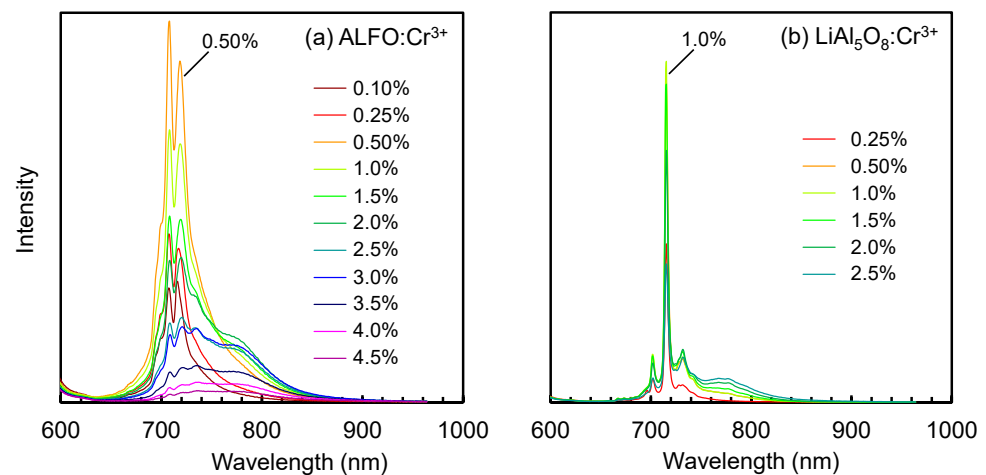


Figure 6. Emission peaks of ALFO:Cr³⁺ (a) and LiAl₅O₈:Cr³⁺ (b) as a function of Cr³⁺ concentration.

LiAl₅O₈:Cr³⁺ showed the maximum intensity at Cr³⁺ = 1.0%, and the change of the overall peak profile was less distinct than ALFO:Cr³⁺. The broad peak around 780 nm also developed in LiAl₅O₈:Cr³⁺ above 1.0%, but the intensity was relatively low.

Figure 7 shows the variation of the internal and external quantum efficiencies (QEs) of ALFO:Cr³⁺ and LiAl₅O₈:Cr³⁺ versus Cr³⁺ concentration. The circles and triangles indicate the internal and external quantum efficiencies QE_{Int} and QE_{Ext}, respectively; the filled and unfilled marks indicate the QEs of ALFO:Cr³⁺ and LiAl₅O₈:Cr³⁺, respectively. ALFO:Cr³⁺ showed higher QEs than LiAl₅O₈:Cr³⁺. The QE_{Int} for ALFO was 85.6% at Cr³⁺ = 0.5%, higher than the maximum QE_{Int} of 58.3% for LiAl₅O₈ at Cr³⁺ = 1.0%. The highest QE_{Ext} was 18.6% for ALFO:Cr³⁺ and 11.6% for LiAl₅O₈:Cr³⁺. The enhancement of QEs of ALFO:Cr³⁺ was attributed to the high crystallinity suggested by the well-developed grains observed in SEM (Figure 3), the disruption of local symmetry around the luminescent center Cr³⁺ from the ideal octahedron with the introduction of F⁻ and vacancies on the O²⁻ sites, and the increased area of the PL peaks due to peak broadening.

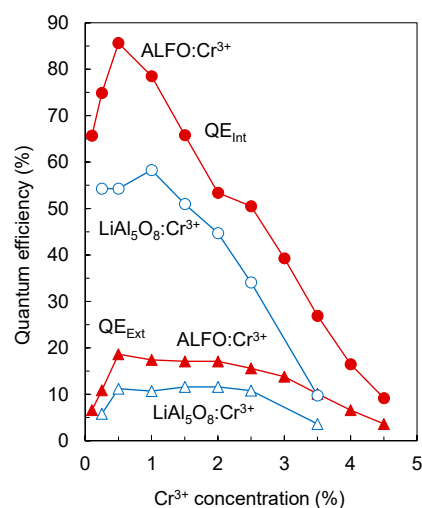


Figure 7. Internal and external quantum efficiencies of ALFO:Cr³⁺ and LiAl₅O₈:Cr³⁺ with different Cr³⁺ concentrations. QE_{Int} and QE_{Ext} represent internal and external quantum efficiencies, respectively.

3.4. Local Environments around Cr³⁺

Cr³⁺ prefers octahedral coordination in the host spinel lattice in both ALFO and LiAl₅O₈, whereas the different spectra suggested different local environments around Cr³⁺ in ALFO and LiAl₅O₈. Such aperiodic local structures are difficult to investigate using

diffraction-based structural analysis, particularly for low-concentration dopants. In fact, the ALFO:Cr³⁺ samples prepared at the different temperatures showed substantially the same XRD patterns (Figure S5 in Supplementary Materials), but the emission peaks varied as shown in Figure 5.

Cr³⁺ in the d³ configuration is an ESR active ion, and the ESR technique was expected to effectively detect the differences in the electronic structures affected by the coordination environment. Figure 8 compares the ESR spectra of 0.5% Cr³⁺ doped α -Al₂O₃ (a), LiAl₅O₈ (b), and ALFO (c) prepared at 1200 °C. Cr³⁺ in α -Al₂O₃ was focused on in the 1960s as a good model example for ESR measurements [44,50–58]. The ESR signal of Cr³⁺ in α -Al₂O₃ (Figure 8a) was consistent with those reported for Cr³⁺ in polycrystalline α -Al₂O₃ in the previous literature [50] and consisted of several peaks corresponding to $g = 3.79$, 2.26, 1.72, and 1.46. For octahedrally coordinated d³ ions placed in a magnetic field, the lowest energy state is the spin quartet, with the spin quantum number $s = -3/2$ along the direction of the magnetic field. The signal of a polycrystalline sample is the average of the spectra of individual crystallites, and the angular dependence of Cr³⁺ in single crystalline Al₂O₃ [59] indicated that the peaks at $g = 3.79$ and 2.26 were assigned to the $s = -3/2$ to $-1/2$ transition, and the peaks at $g = 1.72$ and 1.46 to the $-1/2$ to $+1/2$ transition and $+1/2$ to $+3/2$ transition, respectively (Appendix B) [50,51].

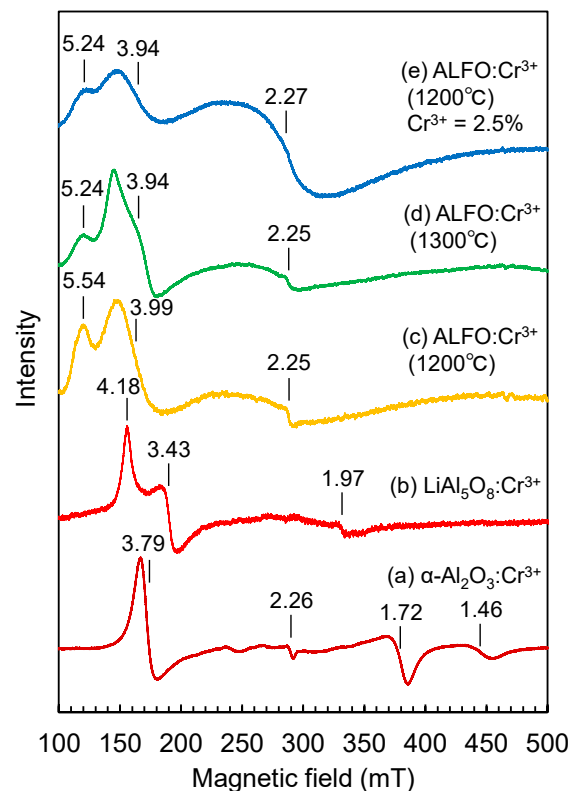


Figure 8. ESR signals of 0.5% Cr³⁺ in (a) α -Al₂O₃, (b) LiAl₅O₈, (c) ALFO prepared at 1200 °C, (d) ALFO prepared at 1300 °C, and (e) ALFO prepared at 1200 °C containing 2.5% Cr³⁺.

Cr³⁺ in LiAl₅O₈ showed essentially the same ESR signal (Figure 8b) as reported by Singh et al. [45] for LiAl₅O₈:Cr³⁺. Singh et al. assigned distinct peaks at $g = 4.03$ and 3.27 and smaller peaks at $g = 5.44$, 4.89, and 4.51 to the isolated Cr³⁺ ions and the resonance signal at $g = 1.97$ to the magnetic interaction between the Cr³⁺ ions, based on the literature [60,61].

The basic features of the ESR signal of Cr³⁺ in ALFO (Figure 8c) were similar to those of Cr³⁺ in LiAl₅O₈ (Figure 8b), but the profiles became broad and the signal positions shifted toward the low magnetic field side. The broadening of the ESR signal was attributed to an inhomogeneous local environment around the Cr³⁺ ions in ALFO. The CrO₆ octahedra in ALFO are expected to be disturbed by the statistical distribution of Al³⁺ and Li⁺ on the

adjacent cation sites. The shift of the ESR signal of ALFO toward the lower field side than LiAl_5O_8 indicated the increased zero-field splitting.

The PL spectra of Cr^{3+} in ALFO prepared at 1100 °C and 1300 °C were apparently similar to that of Cr^{3+} in LiAl_5O_8 , but the ERS signal of Cr^{3+} in ALFO prepared at 1300 °C (Figure 8d) was different from that in LiAl_5O_8 prepared at 1200 °C (Figure 8b), indicating that the similarity in the PL spectra was not due to similar local environments around the luminescent center Cr^{3+} in these host materials.

Increasing the Cr^{3+} concentration to 2.5% resulted in broadening and enhancement of the ESR peak around $g \sim 2.3$ (Figure 8e), which was considered to reflect the magnetic interaction between Cr^{3+} ions, as Singh et al. discussed that $g = 1.95$ was due to exchange coupling of Cr^{3+} - Cr^{3+} pairs [45]. The broadening of the peak at $g \sim 1.96$ with increasing Cr^{3+} concentration was also observed in Cr^{3+} -containing phosphate glasses in the literature [62]. The presence of the magnetic interactions between Cr^{3+} ions at high concentrations was consistent with the discussion of the PL spectra, where the broad shoulder peak developed around 780 nm with increasing Cr^{3+} concentration (Figure 6a).

Since it was difficult to directly deduce the detailed local environment from the ESR signals, the local environment of isolated Cr^{3+} ions is discussed here using MD. The O-Cr-O bond angles of CrO_6 octahedra in $\alpha\text{-Al}_2\text{O}_3$ and ordered LiAl_5O_8 obtained in MD are tabulated in Table S2 in Supplementary Materials.

In $\alpha\text{-Al}_2\text{O}_3$, Cr^{3+} was considered to be placed in a trigonal symmetry as suggested by McClure experimentally [63], which was also reproduced in our MD [39]. The previous literature referred to the rhombic distortion for CrO_6 in LiAl_5O_8 with C_2 symmetry [19,45]. Our MD result indicated that Cr^{3+} was arranged in a monoclinic symmetry that retained a single two-fold axis passing through the midpoints of O1 and O3, and of O5 and O6 (Figure 9b), and the two-fold axis is illustrated on the O1-O3-O6-O5 plane (c). Because of the complexity of the structure, including the disordered arrangement of cations and the presence of vacancies on the anion sites, MD for ALFO has not yet been performed; the local environment around Cr^{3+} in ALFO was inferred to be similar to that in LiAl_5O_8 , but even more disordered.

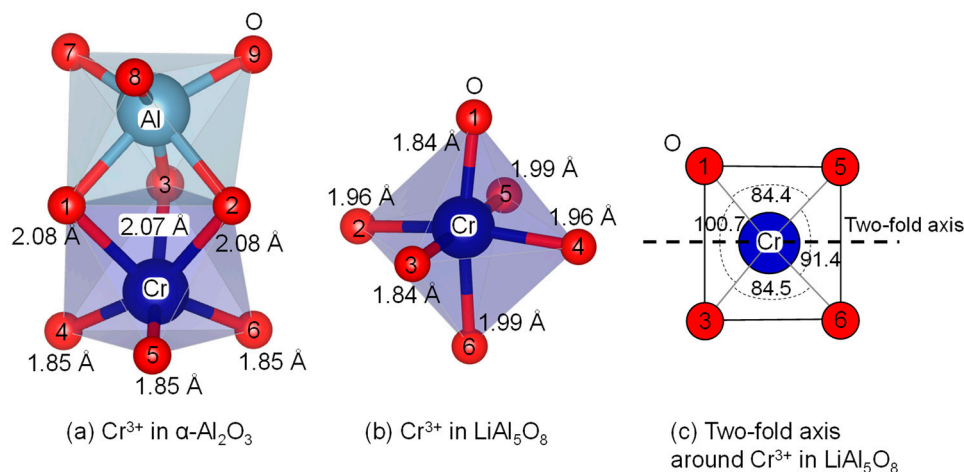


Figure 9. Local coordination environments reproduced by molecular dynamics simulations around Cr^{3+} in $\alpha\text{-Al}_2\text{O}_3$ (a) and LiAl_5O_8 (b). (c) Two-fold axis is shown on the projected O1-O3-O6-O5 plane of the CrO_6 octahedron in (b); note that the bond angles of O1-Cr-O5 (84.4°) and O3-Cr-O6 (84.5°) are not strictly coincident, reflecting thermal vibrations near the equilibrium position of each atom.

4. Conclusions

Fluorine-doped lithium aluminate (ALFO) was prepared from LiF and Al_2O_3 at a ratio of 1:2. ALFO was a fluorine-doped form of LiAl_5O_8 with slightly lithium-rich compositions. The concentration of the incorporated fluorine was dependent on the preparation conditions; the chemical composition varied from $\text{Al}_{4.69}\text{Li}_{1.31}\text{F}_{0.28}\text{O}_{7.55}$ prepared at 1100 °C to $\text{Al}_{4.83}\text{Li}_{1.17}\text{F}_{0.10}\text{O}_{7.78}$ prepared at 1300 °C. ALFO and LiAl_5O_8 were isostructural with

respect to having a spinel-type lattice and they were in a disorder–order relationship, where the regular arrangement of Li^+ and Al^{3+} in ordered LiAl_5O_8 was disordered to a random arrangement with a slight preference of Li^+ on the octahedral sites. The structural difference between ALFO and LiAl_5O_8 resulted in the different PL spectra for Cr^{3+} . Cr^{3+} in ALFO showed deep red emission at around 700 nm, as did Cr^{3+} in LiAl_5O_8 , but the peaks broadened. This was attributed to the disordered arrangement of Li^+ and Al^{3+} on the adjacent cation sites, which led to ununiform local distortion of the CrO_6 octahedra.

In conclusion, a new host material was proposed for deep red phosphors with the luminescent center Cr^{3+} excited by visible rays of blue (~410 nm) and green (~570 nm) light. This work revealed that the structural modification with a small amount of dopant (in this case, fluorine) led to variations in the luminescence properties and enhancement of PL even for the common lattice structure.

Supplementary Materials: The following supporting information can be downloaded at: <https://www.mdpi.com/article/10.3390/ma17020338/s1>, Figure S1: XRD patterns of aluminum lithium fluoride oxide (ALFO) samples prepared at 1100 °C, 1200 °C, and 1300 °C; Figure S2: The result of the Rietveld analysis for non-doped ALFO sample ($\text{Al}_{4.73}\text{Li}_{1.27}\text{F}_{0.17}\text{O}_{7.65}$) prepared at 1200 °C; Figure S3: Perspective view of the crystal structures of ordered LiAl_5O_8 (a) and aluminum lithium fluoride oxide (ALFO) (b) in the range $x = 0.2$ to 0.6 along $\langle 100 \rangle$, illustrating the difference in the arrangement of the tetrahedra and the octahedra in these host materials; Figure S4: XRD patterns of aluminum lithium fluoride oxide (ALFO) samples prepared at 1200 °C with different Cr^{3+} concentrations; Figure S5: XRD patterns of aluminum lithium fluoride oxide (ALFO) samples prepared at different temperatures; Figure S6: Comparison of XRD patterns of disordered spinel (ALFO), ordered spinel (LiAl_5O_8), and partially ordered LiAl_5O_8 prepared by quenching from 1400 °C; Table S1: The structural parameters refined in the Rietveld analysis for non-doped ALFO sample ($\text{Al}_{4.73}\text{Li}_{1.27}\text{F}_{0.17}\text{O}_{7.65}$) prepared at 1200 °C; Table S2: Bond angles in CrO_6 octahedra in $\alpha\text{-Al}_2\text{O}_3$ and ordered LiAl_5O_8 after relaxation by MD; Table S3: Assignment of the ESR peaks of the polycrystalline sample of Cr^{3+} in $\alpha\text{-Al}_2\text{O}_3$.

Author Contributions: Conceptualization, Y.M.; methodology, Y.M., T.T. and M.K.; software, R.H.; validation, Y.M., T.T., M.K., H.K. and K.H.; formal analysis, Y.K., M.K. and Y.M.; investigation, Y.K., M.K., K.U., T.S. and Y.M.; resources, Y.M., H.K., K.H. and M.K.; data curation, Y.K., T.T., M.K. and Y.M.; writing—original draft preparation, Y.K.; writing—review and editing, T.T., M.K., H.K., K.H. and Y.M.; visualization, Y.K., R.H. and Y.M.; supervision, Y.M.; project administration, Y.M.; funding acquisition, Y.M. and K.H. All authors have read and agreed to the published version of the manuscript.

Funding: This research was funded by KAKENHI (20K05658) and the Cooperative Research Project of Research Center for Biomedical Engineering (2021 #2012).

Institutional Review Board Statement: Not applicable.

Informed Consent Statement: Not applicable.

Data Availability Statement: Data are available from the corresponding author upon reasonable request.

Acknowledgments: The authors thank Toshiba Nanoanalysis Co. for contract analysis of the chemical compositions.

Conflicts of Interest: The funders had no role in the design of the study; in the collection, analyses, or interpretation of data; in the writing of the manuscript; or in the decision to publish the results.

Appendix A

According to the previous literature [19,40–42], LiAl_5O_8 underwent the phase transition between the low-temperature ordered (II) and high-temperature disordered (I) forms at 1295 °C. However, in our experiments, quenching of LiAl_5O_8 samples prepared from Li_2CO_3 and $\alpha\text{-Al}_2\text{O}_3$ into liquid nitrogen from 1400 °C did not result in the fully disordered phase of LiAl_5O_8 . The quenching resulted in partial Al^{3+} and Li^+ disorder and reduced the peak intensity originating from the cation ordering, indicated by ▼ in Figure 1 and Figure S6 in Supplementary Materials. Figure S6 in Supplementary Materials compares the XRD

patterns of ordered LiAl_5O_8 prepared at 1400 °C, partially ordered LiAl_5O_8 quenched from 1400 °C, and ALFO. The reason that disordered LiAl_5O_8 was not obtained in this work was that the samples were not started from the nitrate gel precursor [19,40–42], and/or a highly sensitive semiconductor X-ray detector, which is supposed to achieve diffraction intensities 100 times higher than those of conventional scintillation counters [64], was used.

ALFO is similar to disordered LiAl_5O_8 with respect to the random distribution of Li^+ and Al^{3+} on the tetrahedral and octahedral cation sites; the incorporation of fluorine from the starting material LiF specifically leads to disorder in the Al and Li arrangement in ALFO.

Appendix B

According to de Biasi [59], the ESR peaks of a polycrystalline $\alpha\text{-Al}_2\text{O}_3\text{:Cr}^{3+}$ sample occur at $\theta \approx 40^\circ$ and 90° , the angle (θ) between the direction of the applied magnetic field and the z axis. From the angle dependence of the ESR signal of a Cr^{3+} -doped $\alpha\text{-Al}_2\text{O}_3$ single crystal [51], the peaks were assigned as shown in Table S3 in Supplementary Materials.

References

1. Uheda, K.; Hirosaki, N.; Yamamoto, Y.; Naito, A.; Nakajima, T.; Yamamoto, H. Luminescence properties of a red phosphor, $\text{CaAlSiN}_3\text{:Eu}^{2+}$, for white light-emitting diodes. *Electrochem. Solid-State Lett.* **2006**, *9*, H22–H25. [\[CrossRef\]](#)
2. Piao, X.; Machida, K.; Horikawa, T.; Hanzawa, H.; Shimomura, Y.; Kijima, N. Preparation of $\text{CaAlSiN}_3\text{:Eu}^{2+}$ phosphors by the self-propagating high-temperature synthesis and their luminescent properties. *Chem. Mater.* **2007**, *19*, 4592–4599. [\[CrossRef\]](#)
3. Kim, H.S.; Horikawa, T.; Hanzawa, H.; Machida, K. Luminescence properties of $\text{CaAlSiN}_3\text{:Eu}^{2+}$ mixed nitrides prepared by carbothermal process. *J. Phys. Conf. Ser.* **2012**, *379*, 012016. [\[CrossRef\]](#)
4. Daicho, H.; Shinomiya, Y.; Enomoto, K.; Nakano, A.; Sawa, H.; Matsuiishi, S.; Hosono, H. A novel red-emitting $\text{K}_2\text{Ca}(\text{PO}_4)\text{F}\text{:Eu}^{2+}$ phosphor with a large Stokes shift. *Chem. Commun.* **2018**, *54*, 884–887. [\[CrossRef\]](#) [\[PubMed\]](#)
5. Kamimura, M. Recent progress of near-infrared fluorescence in vivo bioimaging in the second and third biological window. *Anal. Sci.* **2021**, *37*, 691–697. [\[CrossRef\]](#) [\[PubMed\]](#)
6. Gil, H.M.; Price, T.W.; Chelani, K.; Bouillard, J.-S.G.; Calaminus, S.D.J.; Stasiuk, G.J. NIR-quantum dots in biomedical imaging and their future. *iScience* **2021**, *24*, 102189. [\[CrossRef\]](#) [\[PubMed\]](#)
7. Piwoński, H.; Nozue, S.; Habuchi, S. The pursuit of shortwave infrared-emitting nanoparticles with bright fluorescence through molecular design and excited-state engineering of molecular aggregates. *ACS Nanosci. Au* **2022**, *2*, 253–283. [\[CrossRef\]](#) [\[PubMed\]](#)
8. Congiu, M.; Alamiry, M.; Moudam, O.; Ciorba, S.; Richardson, P.R.; Maron, L.; Jones, A.C.; Richards, B.S.; Robertson, N. Preparation and photophysical studies of $[\text{Ln}(\text{hfac})_3\text{DPEPO}]$, Ln = Eu, Tb, Yb, Nd, Gd; interpretation of total photoluminescence quantum yields. *Dalton Trans.* **2013**, *42*, 13537–13545. [\[CrossRef\]](#)
9. Tamatani, M. Luminescence centers of transition metal ions. In *Phosphor Handbook*; Shionoya, S., Yen, W.M., Eds.; CRC Press: Boca Raton, FL, USA, 1999; pp. 153–176.
10. Sijbom, H.F.; Verstraete, R.; Joos, J.J.; Poelman, D.; Smet, P.F. $\text{K}_2\text{SiF}_6\text{:Mn}^{4+}$ as a red phosphor for displays and warm-white LEDs: A review of properties and perspectives. *Opt. Mater. Exp.* **2017**, *7*, 3332–3365. [\[CrossRef\]](#)
11. Sankarasubramanian, K.; Devakumar, B.; Annadurai, G.; Sun, L.; Zeng, Y.-J.; Huang, X. Novel $\text{SrLaAlO}_4\text{:Mn}^{4+}$ deep-red emitting phosphors with excellent responsiveness to phytochrome P_{FR} for plant cultivation LEDs: Synthesis, photoluminescence properties, and thermal stability. *RSC Adv.* **2018**, *8*, 30223–30229. [\[CrossRef\]](#)
12. Sun, Q.; Wang, S.; Devakumar, B.; Li, B.; Sun, L.; Liang, J.; Chen, D.; Huang, X. Novel far-red-emitting $\text{SrGdAlO}_4\text{:Mn}^{4+}$ phosphors with excellent responsiveness to phytochrome P_{FR} for plant growth lighting. *RSC Adv.* **2018**, *8*, 39307–39313. [\[CrossRef\]](#) [\[PubMed\]](#)
13. Luchechko, A.; Vasylytsiv, V.; Zhydachevskiy, Y.; Kushlyk, M.; Ubizskii, S.; Suchocki, A. Luminescence spectroscopy of Cr^{3+} ions in bulk single crystalline $\beta\text{-Ga}_2\text{O}_3$. *J. Phys. D Appl. Phys.* **2020**, *53*, 354001. [\[CrossRef\]](#)
14. Wood, D.L.; Imbusch, G.F.; Macfarlane, R.M.; Kisliuk, P.; Larkin, D.M. Optical spectrum of Cr^{3+} ions in spinels. *J. Chem. Phys.* **1968**, *48*, 5255–5263. [\[CrossRef\]](#)
15. Derkosch, J.; Mikenda, W.; Preisinger, A. N-lines and chromium-pairs in the luminescence spectra of the spinels $\text{ZnAl}_2\text{O}_4\text{:Cr}^{3+}$ and $\text{MgAl}_2\text{O}_4\text{:Cr}^{3+}$. *J. Solid State Chem.* **1977**, *22*, 127–133. [\[CrossRef\]](#)
16. Brik, M.G.; Papan, J.; Jovanović, D.J.; Dramićanin, M.D. Luminescence of Cr^{3+} ions in ZnAl_2O_4 and MgAl_2O_4 spinels: Correlation between experimental spectroscopic studies and crystal field calculations. *J. Lumin.* **2016**, *177*, 145–151. [\[CrossRef\]](#)
17. Tran, M.T.; Trung, D.Q.; Tu, N.; Anh, D.D.; Thu, L.T.H.; Du, N.V.; Quang, N.V.; Huyen, N.T.; Kien, N.D.T.; Viet, D.X.; et al. Single-phase far-red-emitting $\text{ZnAl}_2\text{O}_4\text{:Cr}^{3+}$ phosphor for application in plant growth LEDs. *J. Alloys Compd.* **2021**, *884*, 161077. [\[CrossRef\]](#)
18. Lin, Y.; Wu, H.; Wang, C.; Zhang, J.; Yao, Q.; Wu, S.; Hu, Y. Co-precipitation synthesis of $\text{ZnAl}_2\text{O}_4\text{:Cr}^{3+}$ phosphor for better light penetration in pc-LED. *J. Mater. Sci. Mater. Electron.* **2022**, *33*, 19871–19883. [\[CrossRef\]](#)

19. Pott, G.T.; McNicol, B.D. Luminescence of Cr³⁺ ions in ordered and disordered LiAl₅O₈. *J. Solid State Chem.* **1973**, *7*, 132–137. [[CrossRef](#)]
20. Khaidukov, N.M.; Nikonov, K.S.; Brekhovskikh, M.N.; Kirikova, N.Y.; Kondratyuk, V.A.; Makhov, V.N. Low-temperature luminescence of lithium aluminate spinel LiAl₅O₈ doped with chromium ions. *Inorg. Mater.* **2022**, *58*, 751–763. [[CrossRef](#)]
21. Sevast'yanov, B.K.; Sviridov, D.T.; Orekhova, V.P.; Pasternak, L.B.; Sviridova, R.K.; Veremeichik, T.F. Optical absorption spectrum of excited Cr³⁺ ions in yttrium aluminum garnet. *Sov. J. Quantum Electron.* **1973**, *2*, 339. [[CrossRef](#)]
22. Yamaga, M.; Henderson, B.; O'Donnell, K.P.; Yue, G. Temperature dependence of the lifetime of Cr³⁺ luminescence in garnet crystals. *Appl. Phys. B* **1990**, *51*, 132–136. [[CrossRef](#)]
23. Gluchowski, P.; Pazik, R.; Hreniak, D.; Stręk, W. Luminescence properties of Cr³⁺:Y₃Al₅O₁₂ nanocrystals. *J. Lumin.* **2009**, *129*, 548–553. [[CrossRef](#)]
24. Martín-Rodríguez, R.; Valiente, R.; Rodríguez, F.; Bettinelli, M. Temperature and pressure dependence of the optical properties of Cr³⁺-doped Gd₃Ga₅O₁₂ nanoparticles. *Nanotechnology* **2011**, *22*, 265707. [[CrossRef](#)] [[PubMed](#)]
25. Wood, D.L.; Ferguson, J.; Knox, K.; Dillon, J.F., Jr. Crystal-field spectra of d^{3,7} ions. III. Spectrum of Cr³⁺ in various octahedral crystal fields. *J. Chem. Phys.* **1963**, *39*, 890–898. [[CrossRef](#)]
26. Skvortsova, V.; Mironova-Ulmane, N.; Trinkler, L.; Merkulov, V. Optical properties of natural and synthetic beryl crystals. *IOP Conf. Ser. Mater. Sci. Eng.* **2015**, *77*, 012034. [[CrossRef](#)]
27. Liu, G.; Molokeev, M.S.; Xia, Z. Structural rigidity control toward Cr³⁺-based broadband near-infrared luminescence with enhanced thermal stability. *Chem. Mater.* **2022**, *34*, 1376–1384. [[CrossRef](#)]
28. Rajendran, V.; Fang, M.-H.; Huang, W.-T.; Majewska, N.; Lesniewski, T.; Mahlik, S.; Leniec, G.; Kaczmarek, S.M.; Pang, W.K.; Peterson, V.K.; et al. Chromium ion pair luminescence: A strategy in broadband near-infrared light-emitting diode design. *J. Am. Chem. Soc.* **2021**, *143*, 19058–19066. [[CrossRef](#)]
29. Back, M.; Ueda, J.; Brik, M.G.; Lesniewski, T.; Grinberg, M.; Tanabe, S. Revisiting Cr³⁺-doped Bi₂Ga₄O₉ spectroscopy: Crystal field effect and optical thermometric behavior of near-infrared-emitting singly-activated phosphors. *ACS Appl. Mater. Interfaces* **2018**, *10*, 41512–41524. [[CrossRef](#)]
30. Zhou, J.; Xia, Z. Synthesis and near-infrared luminescence of La₃GaGe₅O₁₆:Cr³⁺ phosphors. *RSC Adv.* **2014**, *4*, 46313–46318. [[CrossRef](#)]
31. Zhao, F.Y.; Cai, H.; Zhang, S.Y.; Song, Z.; Liu, Q.L. Octahedron-dependent near-infrared luminescence in Cr³⁺-activated phosphors. *Materialstoday Chem.* **2022**, *23*, 100704. [[CrossRef](#)]
32. Kobayashi, R.; Tamura, H.; Kamada, Y.; Kakihana, M.; Matsushima, Y. A new host compound of aluminum lithium fluoride oxide for deep red phosphors based on Mn⁴⁺, Fe³⁺ and Cr³⁺. *ECS Trans.* **2019**, *88*, 225–236. [[CrossRef](#)]
33. Belov, S.F.; Abaeva, T.I.; Rozdin, I.A.; Varfolomeev, M.B. Reaction of Al₂O₃ with LiF. *Inorg. Mater.* **1984**, *20*, 1675–1676.
34. Takahashi, H.; Takahashi, H.; Watanabe, K.; Kominami, H.; Hara, K.; Matsushima, Y. Fe³⁺ red phosphors based on lithium aluminates and an aluminum lithium oxyfluoride prepared from LiF as the Li Source. *J. Lumin.* **2017**, *182*, 53–58. [[CrossRef](#)]
35. Wang, Q.; Liao, J.; Kong, L.; Qiu, B.; Li, J.; Huang, H.; Wen, H. Luminescence properties of a non-rare-earth doped oxyfluoride LiAl₄O₆F:Mn⁴⁺ red phosphor for solid-state lighting. *J. Alloys Compd.* **2019**, *772*, 499–506. [[CrossRef](#)]
36. Izumi, F.; Momma, K. Three-dimensional visualization in powder diffraction. *Solid State Phenom.* **2007**, *130*, 15–20. [[CrossRef](#)]
37. Momma, K.; Izumi, F. VESTA 3 for three-dimensional visualization of crystal, volumetric and morphology data. *J. Appl. Crystallogr.* **2011**, *44*, 1272–1276. [[CrossRef](#)]
38. Kawamura, K. Environmental Nano-Mechanics-Molecular Simulations. Available online: <https://kats-labo.jimdofree.com/mxdorto-mxdtricl/> (accessed on 25 December 2023).
39. Ichikawa, J.; Kominami, H.; Hara, K.; Kakihana, M.; Matsushima, Y. Electronic structure calculation of Cr³⁺ and Fe³⁺ in phosphor host materials based on relaxed structures by molecular dynamics simulation. *Technologies* **2022**, *10*, 56. [[CrossRef](#)]
40. Datta, R.K.; Roy, R. Phase transitions in LiAl₅O₈. *J. Am. Ceram. Soc.* **1963**, *46*, 388–390. [[CrossRef](#)]
41. Pott, G.T.; McNicol, B.D. Zero-phonon transition and fine structure in the phosphorescence of Fe³⁺ ions in ordered and disordered LiAl₅O₈. *J. Chem. Phys.* **1972**, *56*, 5246–5254. [[CrossRef](#)]
42. McNicol, B.D.; Pott, G.T. Luminescence of Mn ions in ordered and disordered LiAl₅O₈. *J. Lumin.* **1973**, *6*, 320–334. [[CrossRef](#)]
43. Shannon, R.D. Revised effective ionic radii and systematic studies of interatomic distances in halides and chalcogenides. *Acta Crystallogr.* **1976**, *A32*, 751–767. [[CrossRef](#)]
44. Mironova-Ulmane, N.; Brik, M.G.; Grube, J.; Krieke, G.; Kemere, M.; Antuzevics, A.; Gabrusenoks, E.; Skvortsova, V.; Elsts, E.; Sarakovskis, A.; et al. EPR, optical and thermometric studies of Cr³⁺ ions in the α-Al₂O₃ synthetic single crystal. *Opt. Mater.* **2022**, *132*, 112859. [[CrossRef](#)]
45. Singh, V.; Chakradhar, R.P.S.; Rao, J.L.; Kwak, H.-Y. Characterization, EPR and photoluminescence studies of LiAl₅O₈:Cr phosphors. *Solid State Sci.* **2009**, *11*, 870–874. [[CrossRef](#)]
46. Tanabe, Y.; Sugano, S. On the absorption spectra of complex ions. I. *J. Phys. Soc. Jpn.* **1954**, *9*, 753–766. [[CrossRef](#)]
47. Tanabe, Y.; Sugano, S. On the absorption spectra of complex ions II. *J. Phys. Soc. Jpn.* **1954**, *9*, 766–779. [[CrossRef](#)]
48. Tanabe, Y.; Sugano, S. On the absorption spectra of complex ions, III the calculation of the crystalline field strength. *J. Phys. Soc. Jpn.* **1956**, *11*, 864–877. [[CrossRef](#)]
49. Vink, A.P.; De Bruin, M.A.; Roke, S.; Peijzel, P.S.; Meijerink, A. Luminescence of exchange coupled pairs of transition metal ions. *J. Electrochem. Soc.* **2001**, *148*, E313–E320. [[CrossRef](#)]

50. De Biasi, R.S.; Rodrigues, D.C.S. Influence of chromium concentration and particle size on the ESR linewidth of $\text{Al}_2\text{O}_3\text{:Cr}^{3+}$ powders. *J. Mater. Sci.* **1981**, *16*, 968–972. [[CrossRef](#)]
51. Wenzel, R.F.; Kim, Y.W. Linewidth of the electron paramagnetic resonance of $(\text{Al}_2\text{O}_3)_{1-x}(\text{Cr}_2\text{O}_3)_x$. *Phys. Rev.* **1965**, *140*, A1592–A1598. [[CrossRef](#)]
52. Grant, W.J.C.; Strandberg, M.W.P. Line shapes of paramagnetic resonances of chromium in ruby. *Phys. Rev.* **1964**, *135*, A727–A739. [[CrossRef](#)]
53. Manenkov, A.A.; Prokhorov, A.M. The fine structure of the spectrum of the paramagnetic resonance of the ion Cr^{3+} in Chromium corundum. *Sov. Phys.-JETP* **1955**, *1*, 611.
54. Zaripov, M.M.; Shamonin, I.I. Paramagnetic resonance in synthetic ruby. *Sov. Phys.-JETP* **1956**, *3*, 171–175.
55. Geusic, J.E. Paramagnetic fine structure spectrum of Cr^{+++} in a single ruby crystal. *Phys. Rev.* **1956**, *102*, 1252–1253. [[CrossRef](#)]
56. Manenkov, A.A.; Prokhorov, A.M. Hyperfine structure of the paramagnetic resonance spectrum of $^{53}\text{Cr}^{3+}$ in Al_2O_3 . *Sov. Phys.-JETP* **1957**, *4*, 288–289.
57. Zverev, G.M.; Prokhorov, A.M. Fine structure and hyperfine structure of paramagnetic resonance of Cr^{+++} in synthetic ruby. *Sov. Phys.-JETP* **1958**, *7*, 354–355.
58. Schulz-Du Bois, E.O. Paramagnetic spectra of substituted sapphires—Part I: Ruby. *Bell Syst. Tech. J.* **1959**, *38*, 271–290. [[CrossRef](#)]
59. De Biasi, R.S.; Rodrigues, D.C.S. Measurement of small concentrations of Cr and Fe in $\alpha\text{-Al}_2\text{O}_3$ using electron spin resonance. *J. Am. Ceram. Soc.* **1985**, *68*, 409–412. [[CrossRef](#)]
60. Orton, J.W. *Electron Paramagnetic Resonance: An introduction to Transition Group Ions in Crystals*; ILIFFE Book Ltd.: London, UK, 1968.
61. Ardelean, I.; Ilonca, G.; Peteanu, M.; Barbos, E.; Indrea, E. EPR and magnetic susceptibility studies of $x\text{Cr}_2\text{O}_3\text{-(1-x)3B}_2\text{O}_3\text{-PbO}$ glasses. *J. Mater. Sci.* **1982**, *17*, 1988–1996. [[CrossRef](#)]
62. Landry, R.J.; Fournier, J.T.; Young, C.G. Electron spin resonance and optical absorption studies of Cr^{3+} in a phosphate glass. *J. Chem. Phys.* **1967**, *46*, 1285–1290. [[CrossRef](#)]
63. McClure, D.S. Optical spectra of transition-metal ions in corundum. *J. Chem. Phys.* **1962**, *36*, 2757–2779. [[CrossRef](#)]
64. Rigaku Co. Measurement of Trace Components Using D/teX Ultra. Available online: <https://japan.rigaku.com/en/applications/bytes/xrd/miniflex/1302286925> (accessed on 25 December 2023).

Disclaimer/Publisher’s Note: The statements, opinions and data contained in all publications are solely those of the individual author(s) and contributor(s) and not of MDPI and/or the editor(s). MDPI and/or the editor(s) disclaim responsibility for any injury to people or property resulting from any ideas, methods, instructions or products referred to in the content.